

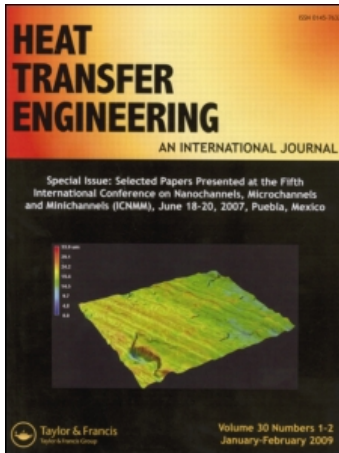
This article was downloaded by: [TÜBTAK EKUAL]

On: 6 May 2009

Access details: Access Details: [subscription number 772815469]

Publisher Taylor & Francis

Informa Ltd Registered in England and Wales Registered Number: 1072954 Registered office: Mortimer House, 37-41 Mortimer Street, London W1T 3JH, UK



## Heat Transfer Engineering

Publication details, including instructions for authors and subscription information:

<http://www.informaworld.com/smpp/title-content=t713723051>

### 1st and 2nd Law Characteristics in a Micropipe: Integrated Effects of Surface Roughness, Heat Flux and Reynolds Number

A. Alper Ozalp<sup>a</sup>

<sup>a</sup> Department of Mechanical Engineering, University of Uludag, Bursa, Turkey

Online Publication Date: 01 January 2009

**To cite this Article** Ozalp, A. Alper(2009)'1st and 2nd Law Characteristics in a Micropipe: Integrated Effects of Surface Roughness, Heat Flux and Reynolds Number',Heat Transfer Engineering,30:12,973 — 987

**To link to this Article:** DOI: 10.1080/01457630902837467

**URL:** <http://dx.doi.org/10.1080/01457630902837467>

PLEASE SCROLL DOWN FOR ARTICLE

Full terms and conditions of use: <http://www.informaworld.com/terms-and-conditions-of-access.pdf>

This article may be used for research, teaching and private study purposes. Any substantial or systematic reproduction, re-distribution, re-selling, loan or sub-licensing, systematic supply or distribution in any form to anyone is expressly forbidden.

The publisher does not give any warranty express or implied or make any representation that the contents will be complete or accurate or up to date. The accuracy of any instructions, formulae and drug doses should be independently verified with primary sources. The publisher shall not be liable for any loss, actions, claims, proceedings, demand or costs or damages whatsoever or howsoever caused arising directly or indirectly in connection with or arising out of the use of this material.

# 1st and 2nd Law Characteristics in a Micropipe: Integrated Effects of Surface Roughness, Heat Flux and Reynolds Number

A. ALPER OZALP

Department of Mechanical Engineering, University of Uludag, Bursa, Turkey

*A computational study of the integrated effects of surface roughness, heat flux, and Reynolds number on the 1st and 2nd law characteristics of laminar-transitional flow in a micropipe is presented. Analyses are carried by solving the variable fluid property continuity, Navier–Stokes, and energy equations for the surface roughness, heat flux, and Reynolds number ranges of 1–50  $\mu\text{m}$ , 5–100  $\text{W}/\text{m}^2$ , and 1–2000, respectively. Computations put forward that surface roughness not only accelerates transition to lower Reynolds number but also augments heat transfer rates, such that the transitional Reynolds numbers and intermittency values are evaluated as  $\sim 1650$ ,  $\sim 575$ , and  $\sim 450$  and 0.132, 0.117, and 0.136 for the surface roughness cases of 1, 20, and 50  $\mu\text{m}$ , respectively. Thermocritical Reynolds numbers are identified by determining the viscous dissipation rates, which characterize the heating/cooling behavior and the related Reynolds number range. Surface roughness comes out to have no role on entropy generation at low Reynolds numbers; moreover, entropy generation is found to be inversely proportional with mean temperature variation, where the trends become almost asymptotic at the lower limit of the investigated Reynolds number range. Being independent of surface roughness, heat flux, and Reynolds number, radial irreversibility distribution ratio is determined to be negligible at the pipe centerline, indicating that the frictional entropy is minor and the major portion of the total entropy generation is thermal based.*

## INTRODUCTION

In many engineering installations internal flows with heat transfer widely take place, and are thus studied extensively. From the scientific point of view, flow and heat transfer characteristics of internal laminar flows are very well known and can be explicitly defined with analytical solutions. However, existence of surface roughness not only leads to considerable deviations in the velocity and temperature profiles from those of the laminar-analytical but also causes the growth of entropy generation, which makes the energy-saving aspects very important in the design, construction, and operation of systems with internal flows. Energy–exergy analysis is defined as a method of performing system analysis according to the conservation of mass, momentum, and energy, and the 2nd law of thermodynamics. It consists of using the 1st and 2nd

law together, and has recently been the topic of great interest in various thermo-fluid operations such as geothermal district heating systems [1], operations with non-Newtonian fluids [2], heat exchangers [3], and even micropipe systems [4].

There exist several published reports of the experimental and numerical investigations on heat and momentum transfer studies of laminar-transitional flows, with surface roughness application, in the last decade. Kandlikar et al. [4] studied the effects of surface roughness on pressure drop and heat transfer in circular tubes, for single-phase flow with small hydraulic diameters, and concluded that transition to turbulent flows occurs at Reynolds number values much below 2300. Experimental investigations of Vicente et al. [5] on dimpled tubes for laminar and transition flows pointed out that the roughness-induced friction factors were 10% higher than the smooth tube ones and the transition onset was at a relatively low Reynolds number of 1400. Guo and Li [6] studied surface-roughness-provoked surface friction; they reported that frictional activity is responsible for the early transition from laminar to turbulent flow. Augmentation

Address correspondence to Professor A. Alper Ozalp, Department of Mechanical Engineering, University of Uludag, 16059 Gorukle, Bursa, Turkey. E-mail: aozalp@uludag.edu.tr

characteristics of heat transfer and pressure drop by the imposed wall heat flux, mass flux, and different strip-type inserts in small tubes were experimentally investigated by Wen et al. [7]. Obot [8] prepared a literature review on friction and heat/mass transfer in microchannels. According to the available literature on microchannels, the arbitrary definition of microchannels is given with a hydraulic diameter of  $D_h \leq 1000 \mu\text{m}$  (1 mm). The main findings are: (i) Onset of transition to turbulent flow in smooth microchannels does not occur if the Reynolds number is less than 1000, and (ii) Nusselt number varies as the square root of the Reynolds number in laminar flow. Engin et al. [9] also considered wall roughness effects in microtube flows; they determined significant departures from the conventional laminar flow theory. The rise of laminar Nusselt number and apparent friction coefficient with the increase of surface roughness were reported by Wu and Cheng [10]; they additionally determined that the increase rates become more obvious at larger Reynolds numbers. As Morini [11] worked on the role of the cross-sectional geometry on viscous dissipation and the minimum Reynolds number for which viscous dissipation effects can not be neglected, Koo and Kleinstreuer [12] numerically and experimentally investigated the significance of viscous dissipation on the temperature field and on the friction factor. The following works of Celata et al. [13, 14] described the roles of surface roughness on viscous dissipation, the resulting earlier transitional activity, and augmented friction factor values and head loss data.

Entropy generation and 2nd law analysis have direct contribution to system performance, reliability, and efficiency for long-term applications. Thus, associated investigations, on internal fluid flow-related problems, have become more frequent recently. The existence of an optimum laminar flow regime in singly connected microchannels with finite temperature differences and fluid friction, based on 2nd law analysis, was investigated by Richardson et al. [15]. Ratts and Raut [16] obtained optimal Reynolds numbers for single-phase, convective, fully developed internal laminar and turbulent flows with uniform heat flux, by employing the entropy generation minimization method. Laminar forced convection and entropy generation in a helical coil with constant wall heat flux was numerically investigated by Ko [17]. He suggested that the optimal Reynolds number is to be chosen according to the flow operating condition so that the thermal system can have the least irreversibility and best exergy utilization. Ko [18] also numerically performed the thermal design of plate heat exchanger double-sine ducts, from the point of entropy generation and exergy utilization. Entropy generation for a fully developed laminar viscous flow in a duct subjected to constant wall temperature was analytically investigated by Sahin [19]. His determinations shown that for low heat transfer conditions, the entropy generation due to viscous friction becomes dominant and the dependence of viscosity on temperature becomes essentially important in accurately determining the entropy generation. Kotas et al. [20] not only shown that the concept of exergy is dependent on that of the environment, but also indicated that for calculating loss of exergy, or

process irreversibility, an exergy balance or the Gouy–Stodola theorem can be used.

Some recent studies concentrated on the roughness definition and roles of roughness on the flow and heat transfer performances of various applications, due to the significant role of surface roughness in thermo-fluid systems. A few of the most recent roughness-based research studies can be summarized as: the numerical works of Ozalp [21, 2] on compressible flow in converging and aerospace propulsion nozzles with various surface roughness conditions, the Sheikh et al. [23] model to eliminate the discrepancy in the fouling measurements by characterizing the fouling as a correlated random process, the Wang et al. [24] regular perturbation method to investigate the influence of two-dimensional roughness on laminar flow in microchannels between two parallel plates, the nonequilibrium molecular dynamics simulation of Cao et al. [25] to investigate the effect of the surface roughness on slip flow of gaseous argon, and the Sahin et al. [26] study on entropy generation due to fouling as compared to that for clean surface tubes.

Despite the several numerical and experimental reports on the fluid motion and heat transfer mechanisms of fluid flow in circular ducts, there still exists the necessity to carry out a work that develops a complete overview on the 1st and 2nd law characteristics of laminar-transitional flow in a micropipe. The current computational study is structured to provide a detailed insight on the momentum transfer, heat transfer, and 2nd law characteristics of roughness-induced forced convective laminar-transitional micropipe flow, for wide ranges of surface roughness, heat flux, and Reynolds number. To simulate real-time micropipe systems, surface roughness data are adopted from the literature. Moreover, the heat flux range is decided by considering the level of entropy generation and so occurring energy loss from the system, such that both heating and cooling scenarios can be investigated. The results on momentum transfer are discussed through radial distributions of axial velocity, boundary layer parameters, and friction coefficients. Heat transfer records are presented in terms of radial temperature profiles, mean temperature variations, Nusselt numbers, and frictional energy loss data to identify the viscous dissipation rates. Second law characteristics are displayed with thermal, frictional, and overall entropy generation rates, by cross-correlating with mass flow rate, mean temperature variations, and Reynolds number. Moreover, radial and overall variation styles of irreversibility distribution ratio and interactions of frictional and thermal entropy values are also established.

## **THEORETICAL BACKGROUND**

### ***Micropipe and Roughness***

The diameter and length of the micropipe (Figure 1a), analyzed in this article, are given as  $D$  and  $L$ . The present roughness model is based on the triangular structure of Cao et al. [25] (Figure 1b), where the roughness amplitude and period are

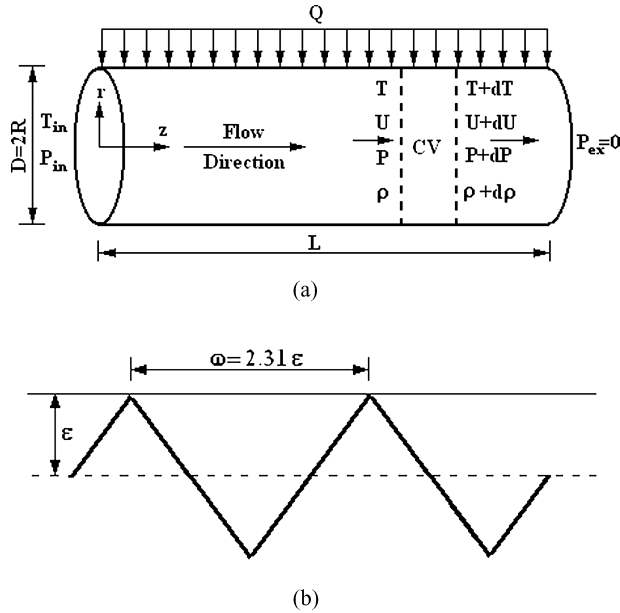


Figure 1 (a) Schematic view of micropipe, (b) triangular surface roughness distribution.

characterized by  $\epsilon$  and  $\omega$ , respectively. The role of roughness on the 1st and 2nd law characteristics of laminar-transitional flow is investigated by varying the amplitude in the range of  $\epsilon = 1\text{--}50\ \mu\text{m}$ . However, in all computations the roughness periodicity parameter ( $\omega' = \omega/\epsilon$ ) is kept fixed to  $\omega' = 2.31$ , which corresponds to equilateral triangle structure (Cao et al. [25]). Equation (1) numerically characterizes the model of Cao et al. [25] with the implementation of the amplitude and period. The model function ( $f_\epsilon(z)$ ) is repeated in the streamwise direction throughout the pipe length, where the Kronecker unit tensor ( $\delta_i$ ) attains the values of  $\delta_1 = +1$  and  $-1$  for  $0 \leq z \leq \frac{2.31}{2}\epsilon$  and  $\frac{2.31}{2}\epsilon \leq z \leq \epsilon \cdot 2.31$ , respectively.

$$f_\epsilon(z) = \delta_i \epsilon \left[ 1 - \frac{4}{2.31} z \right] \quad (1)$$

**Governing Equations**

The average density and velocity of the flow at any cross section of the duct are defined as  $\rho_o$  and  $U_o$ , and  $\nu$  ( $= \mu/\rho$ ) and  $\mu$  are the kinematic and dynamic viscosity, respectively. As the surface and mean flow temperatures are denoted by  $T_s$  and  $T_o$ , thermal conductivity and convective heat transfer coefficient are characterized by  $\kappa_f$  and  $h$ . Using these definitions, Reynolds number and Nusselt number are given by Eqs. (2a) and (2b). Air has been selected as the working fluid in the present study, and the compressible character is handled by the ideal gas formula of  $\rho = \frac{P}{RT}$ . It is well known that air properties, like specific heat at constant pressure ( $C_p$ ), kinematic viscosity ( $\nu$ ), and thermal conductivity ( $\kappa_f$ ), are substantially dependent on temperature (Incropera and DeWitt [27]). To comprehensively implement the property ( $\xi$ ) variations with temperature into the calculations,

the necessary air data of Incropera and DeWitt [27] are fitted into sixth-order polynomials, which can be presented in closed form by Eq. (2c). The uncertainty of the fitted air data is less than 0.02% and the temperature dependency is indicated by the superscript T throughout the formulation.

$$\text{Re} = \frac{U_o D}{\nu^T} = \frac{\rho_o U_o D}{\mu^T} \quad (a) \quad \text{Nu} = \frac{hD}{\kappa_f^T} = \frac{\partial T / \partial r|_{r=R} D}{T_s - T_o}$$

$$(b) \quad \zeta^T = \sum_{j=0}^6 a_j T^j \quad (c) \quad (2)$$

The problem considered here is steady ( $\partial/\partial t = 0$ ), fully developed, and the flow direction is coaxial with pipe centerline ( $U_r = U_\theta = 0$ ); thus the velocity vector simplifies to  $\vec{V} = U_z(r,z)\hat{k}$ , denoted  $\partial U_z / \partial \theta = 0$ . These justifications are common in several recent numerical studies, on roughness-induced flow and heat transfer investigations, like those of Engin et al. [9], Koo and Kleinstreuer [12], and Cao et al. [25]. The flow boundary conditions are based on the facts that on the pipe wall no-slip condition and constant heat flux exist, and flow and thermal values are maximum at the centerline. As given in Figure 1a, at the pipe inlet, pressure and temperature values are known and the exit pressure is atmospheric. Denoting  $U_z = U(r,z)$  and  $T = T(r,z)$ , the boundary conditions can be summarized as follows:

$$r = R + f_\epsilon(z) \rightarrow U = 0 \quad \& \quad r = 0 \rightarrow \frac{\partial U}{\partial r} = 0$$

$$r = R + f_\epsilon(z) \rightarrow \frac{\partial T}{\partial r} = -\frac{q_r''}{\kappa_f^T} \quad \& \quad r = 0 \rightarrow \frac{\partial T}{\partial r} = 0 \quad (3)$$

$$z = 0 \rightarrow P = P_{in}, T = T_{in} \quad \& \quad z = L \rightarrow P = 0 \text{ (Manometric)}$$

As the components of the viscous stress tensor ( $\tau$ ) and heat flux terms ( $q''$ ) can be written as Eqs. (4) and (5), internal and kinetic energy terms are defined as  $e = C_v T$  and  $k = U_z^2/2$ , respectively.

$$\tau_{rz} = \mu^T \frac{\partial U_z}{\partial r} \quad (a) \quad \tau_{zz} = \frac{4}{3} \mu^T \frac{\partial U_z}{\partial z} \quad (b) \quad (4)$$

$$q_r'' = -\kappa_f^T \frac{\partial T}{\partial r} \quad (a) \quad q_z'' = -\kappa_f^T \frac{\partial T}{\partial z} \quad (b) \quad (5)$$

With these problem definitions and above implementations, for laminar compressible flow with variable fluid properties, continuity, momentum, and energy equations are given as:

$$\frac{\partial}{\partial z}(\rho U_z) = 0 \quad (6)$$

$$\rho \left( U_z \frac{\partial U_z}{\partial z} \right) + \frac{\partial P}{\partial z} = \frac{1}{r} \frac{\partial}{\partial r} (r \tau_{rz}) + \frac{\partial \tau_{zz}}{\partial z} \quad (7)$$

$$\frac{\partial}{\partial z} \left[ \rho \left( e + \frac{P}{\rho} + k \right) U_z \right] + \frac{1}{r} \frac{\partial}{\partial r} (r q_r'') + \frac{\partial q_z''}{\partial z} = \tau_{zz} \frac{\partial U_z}{\partial z} + \tau_{rz} \frac{\partial U_z}{\partial r} + U_z \left[ \frac{1}{r} \frac{\partial}{\partial r} (r \tau_{rz}) + \frac{\partial \tau_{zz}}{\partial z} \right] \quad (8)$$

The average fluid velocity and temperature, at any cross section in the pipe, are obtained from

$$U_o(z) = \frac{2\pi \int_{r=0}^{r=R} \rho(r, z)U(r, z)rdr}{\rho_o \pi R^2} \quad (a)$$

$$T_o(z) = \frac{2\pi \int_{r=0}^{r=R} \rho(r, z)U(r, z)C_p(r, z)T(r, z)rdr}{\rho_o U_o (C_p)_o \pi R^2} \quad (b) \quad (9)$$

and the shear stress and mass flow rate are defined as

$$\tau = C_f \frac{1}{2} \rho_o U_o^2 = \mu^T \left| \frac{dU}{dr} \right|_{r=R} \quad (a)$$

$$\dot{m} = \rho_o U_o A = 2\pi \int_{r=0}^{r=R} \rho(r, z)U(r, z)rdr \quad (b) \quad (10)$$

$$S''' = \frac{\kappa_f^T}{T^2} \left[ \left( \frac{\partial T}{\partial r} \right)^2 + \left( \frac{\partial T}{\partial z} \right)^2 \right] + \frac{\mu^T}{T} \left[ \left( \frac{\partial U}{\partial r} \right)^2 + 2 \left( \frac{\partial U}{\partial z} \right)^2 \right] \quad (a)$$

$$S''' = S'''_{\Delta T} + S'''_{\Delta P} \quad (b) \quad (11)$$

The Gouy–Stodola theorem [20] considers the lost available work to be directly proportional to entropy generation, which results from the nonequilibrium phenomenon of exchange of energy and momentum within the fluid and at the solid boundaries. Due to the existence of the velocity and temperature gradients in the flow volume, the volumetric entropy generation rate is positive and finite. Computation of the temperature and the velocity fields through Eqs. (6)–(8) on the problem domain will produce the input data for Eq. 11(a), which defines the local rate of entropy generation per unit volume ( $S'''$ ), for a two-dimensional ( $r, z$ ) compressible Newtonian fluid flow in cylindrical coordinates.

As given in Eq. 11(b), the entropy generation due to finite temperature differences ( $S'''_{\Delta T}$ ) in axial  $z$  and in radial  $r$  directions is defined by the first term on the right side of Eq. 11(a), the second term stands for the frictional entropy generation ( $S'''_{\Delta P}$ ). As the total values of the frictional, thermal and overall entropy generation rates can be obtained by Eqs. 12(a)–(c), Eqs. 13(a) and 13(b) stand for the local and overall irreversibility distribution ratios.

$$S_{\Delta P} = 2\pi \int_{z=0}^{z=L} \int_{r=0}^{r=R} S'''_{\Delta P} r dr dz \quad (a)$$

$$S_{\Delta T} = 2\pi \int_{z=0}^{z=L} \int_{r=0}^{r=R} S'''_{\Delta T} r dr dz \quad (b)$$

$$S = 2\pi \int_{z=0}^{z=L} \int_{r=0}^{r=R} S''' r dr dz \quad (c) \quad (12)$$

$$\phi''' = \frac{S'''_{\Delta P}}{S'''_{\Delta T}} \quad (a) \quad \phi = \frac{S_{\Delta P}}{S_{\Delta T}} \quad (b) \quad (13)$$

### Computational Method

Laminar micropipe flow with surface roughness and heat flux governs the complete equation set described in the previous section, equations that are highly dependent nonlinear formulations, where the convergence problems and singularities are most likely to occur in the solution scheme of the sufficiently complex structure. Forward difference discretization is applied in the axial and radial directions, for the two-dimensional marching procedure. The flow domain of Figure 1a is divided into  $m$  axial and  $n$  radial cells ( $m \times n$ ), where the fineness of the computational grids is examined to ensure that the obtained solutions are independent of the grid employed. Since the computational findings must be independent of the employed number of cells, optimum meshing is determined by performing several successive runs. These runs indicated an optimum axial cell number of  $m = 500$ , having an equal width of  $\Delta z$ , whereas the radial direction is divided into  $n = 100$  cells. Since the velocity and temperature gradients are significant on the pipe walls, the 20% of the radial region, neighboring solid wall, is employed an adaptive meshing with radial-mesh width aspect ratio of 1.1. For simultaneous handling, Eqs. (6)–(8) need to be assembled into the three-dimensional “transfer matrix,” consisting of the converted explicit forms of the principle equations. The direct simulation Monte Carlo (DSMC) method, as applied by Ozalp [21, 22] to compressible nozzle flow problems and in a similar way by Wu and Tseng [28] to a microscale gas dynamics domain, is a utilized technique especially for internal gas flow applications with instabilities. The DSMC method can couple the influences of surface roughness and surface heat flux conditions over the meshing intervals of the flow domain. The benefits become apparent either when the initial guesses on inlet pressure and inlet velocity do not result in convergence within the implemented mesh, or when the converged solution does not point out the desired Reynolds number in the pipe. There exists two types of convergence problems (singularities) such that (i) Mach number exceeds 1 inside the pipe and (ii) the exit Mach number is lower than or equal to 1 but the exit pressure deviates from the related boundary condition more than 0.01 Pa. [Eq. (3)]. Moreover, as defined in detail by Ozalp [29], to enable the application of different types of boundary conditions with less specific change in programming, cell-by-cell transport tracing technique is adopted to support the “transfer matrix” scheme and to the DSMC algorithm. The concept of triple transport conservation is incorporated into the DSMC, which makes it possible to sensitively evaluate the balance of heat swept from the micropipe walls and the energy transferred in the flow direction and also to perform accurate simulation for inlet/exit pressure boundaries. By simultaneously conserving mass flux and boundary pressure matching within the complete mesh,

thermal equilibrium is satisfied at each pressure boundary in the flow volume. Computations are based on the preconditions that maximum allowable deviation of the exit pressure from the related boundary condition [Eq. (3)] is less than 0.01 Pa and the convergence criteria for the mass flow rate throughout the flow volume is in the order of 0.01%. To investigate the streamwise variations of the three primary flow parameters (U, P, T), the resulting nonlinear system of equations is solved by using the Newton–Raphson method. In the case of a convergence problem, U, P, and T are investigated up to the singularity point, and then the local velocity is compared with the inlet value together with the location of the singularity point with respect to the inlet and exit planes. The inlet velocity is then modified by DSMC, by considering the type of singularity, the velocity variation, and the corresponding pipe length. However, inlet pressure and velocity are both modified, to increase or decrease the Reynolds number of the former iteration step, in the case that the Reynolds number does not fit the required value.

**RESULTS AND DISCUSSION**

Consistent with the microchannel definition of Obot [8], investigations are performed for a micropipe having a diameter of  $D = 1$  mm. To develop a complete overview on the 1st and 2nd law characteristics of laminar-transitional flow and to investigate the integrated effects of surface roughness, heat flux, and Reynolds number, computations are carried out with the sufficiently wide ranges of  $\varepsilon = 1\text{--}50$   $\mu\text{m}$  ( $\varepsilon^* = \varepsilon/D = 0.001\text{--}0.05$ ),  $q'' = 5\text{--}100$   $\text{W/m}^2$ , and  $Re = 1\text{--}2000$ . As the employed surface roughness values are similar to those of Engin et al. [9] ( $\varepsilon^* \leq 0.08$ ), Wang et al. [24] ( $\varepsilon^* = 0.005\text{--}0.05$ ), and Sahin et al. [26] ( $\varepsilon^* \leq 0.25$ ), the applied heat flux range is decided in conjunction with the total entropy generation rates to construct both heating and cooling scenarios. Throughout the work, inlet air temperature, exit pressure, and pipe length are kept fixed at  $T_{in} = 278$  K,  $P_{ex} = 0$ , and  $L = 0.5$  m, respectively. First law analyses are discussed with the two subheadings of momentum and heat transfer characteristics. Second law analyses are presented not only with entropy generation values, by cross-correlating with mass flow rate, mean-temperature variations, and Reynolds number, but also with irreversibility distribution ratio, by demonstrating both the radial and overall variation styles.

**1ST LAW ANALYSES**

**Momentum Transfer Characteristics**

Laminar flow characteristics in a circular micropipe with wall roughness and heat flux conditions are given in terms of radial distributions of axial velocity profiles (VP) (Figure 2), normalized friction coefficients ( $C_f^*$ ) (Figure 3), and tabulated boundary layer parameters (Table 1). Computational outputs showed that varying the level of applied heat flux values had no influence on the VP formation and  $C_f^*$  variation; therefore,

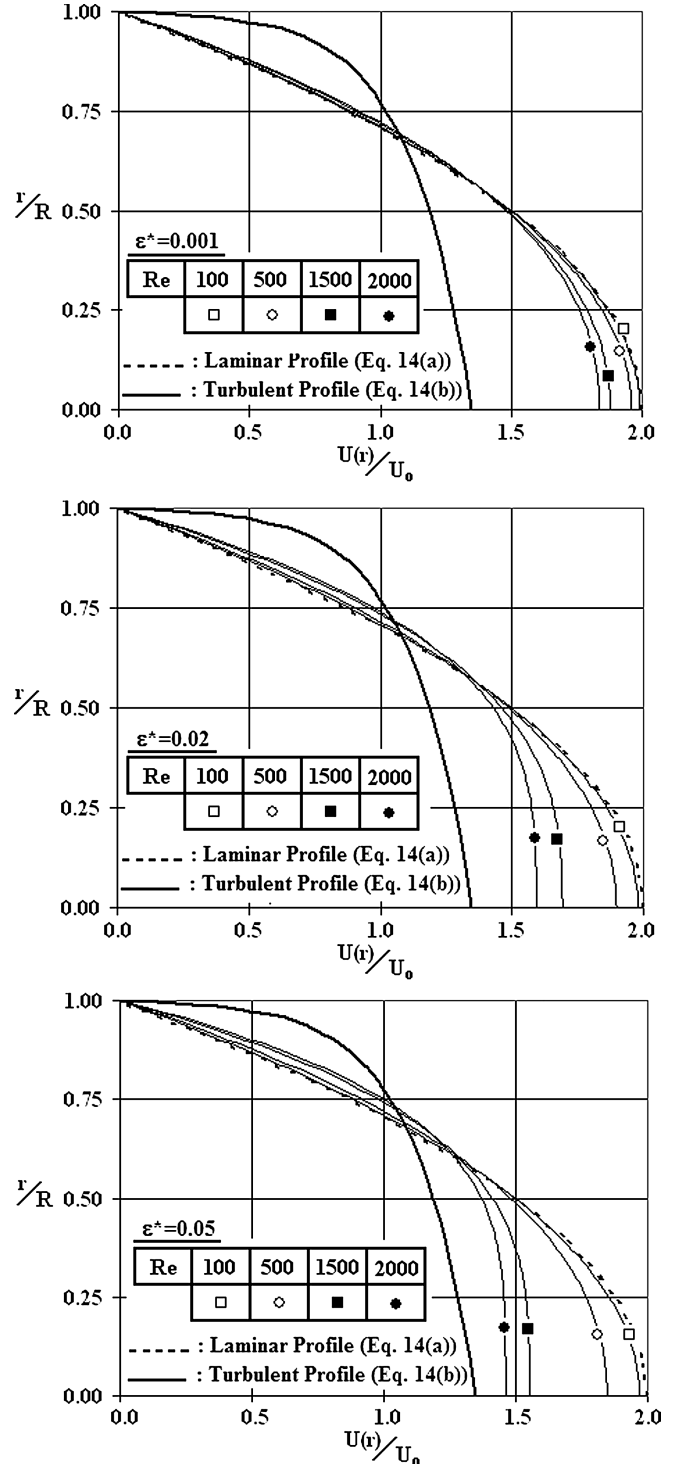


Figure 2 Variation of radial distributions of axial velocity with Re and  $\varepsilon^*$ .

the plotted velocity profiles and normalized friction coefficient data put forward the combined impacts of surface roughness and Reynolds number on the flow characteristics. Moreover, computations pointed to a maximum Mach number of  $M = 0.083$  at the upper Reynolds number limit of  $Re = 2000$ , resulting in a streamwise density variation of 2.42%; thus, the sketched

Downloaded By: [TUBTAK EKUAL] At: 08:49 6 May 2009

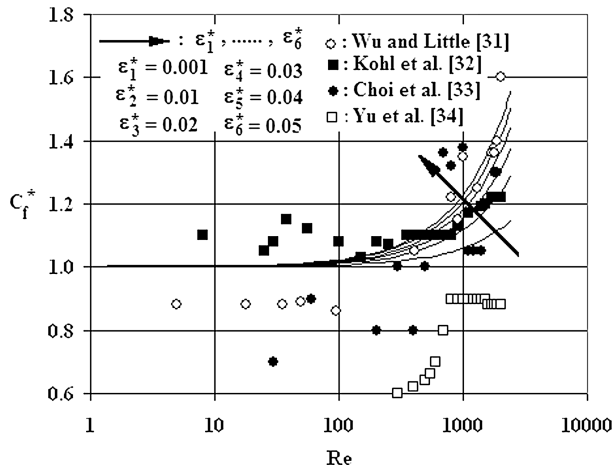


Figure 3 Variation of  $C_f^*$  with  $Re$  and  $\epsilon^*$ .

and tabulated flow characteristics stand for the complete pipe length.

In order to clearly display the deviations of the VPs from the characteristic styles of laminar and turbulent regimes and also to put forward the roles of  $\epsilon$  and  $Re$  on the transition mechanism, the characteristic laminar profile [Eq. (14a)] and the modified turbulent logarithm law for roughness [Eq. (14b)] (White [30]) are also displayed in Figure 2, where  $U^*$  is the friction velocity [Eq. (14c)]. To clarify the role of surface roughness on the frictional activity, the classical and normalized friction coefficient values are evaluated by Eqs. (15a)–(c) (White [30]).

$$\frac{U(r)}{U_o} = 2 \left[ 1 - \left( \frac{r}{R} \right)^2 \right] \quad (a)$$

$$\frac{U(r)}{U^*} = 2.44 \ln \left( \frac{R-r}{\epsilon} \right) + 8.5 \quad (b) \quad U^* = \sqrt{\frac{\tau_w}{\rho}} \quad (c)$$

(14)

Table 1 Boundary layer parameters for various  $Re$  and  $\epsilon^*$  cases

	H	$\gamma$	$C_f$	$C_f^*$
Re = 100				
$\epsilon_1^* = 0.001$	3.35	0.007	0.161	1.006
$\epsilon_2^* = 0.02$	3.33	0.020	0.162	1.016
$\epsilon_5^* = 0.05$	3.31	0.031	0.163	1.021
Re = 500				
$\epsilon_1^* = 0.001$	3.29	0.041	0.033	1.028
$\epsilon_2^* = 0.02$	3.19	0.104	0.035	1.078
$\epsilon_5^* = 0.05$	3.11	0.151	0.036	1.116
Re = 1500				
$\epsilon_1^* = 0.001$	3.16	0.121	0.012	1.088
$\epsilon_2^* = 0.02$	2.91	0.271	0.013	1.228
$\epsilon_5^* = 0.05$	2.81	0.333	0.010	1.350
Re = 2000				
$\epsilon_1^* = 0.001$	3.10	0.158	0.009	1.125
$\epsilon_2^* = 0.02$	2.81	0.333	0.010	1.250
$\epsilon_5^* = 0.05$	2.66	0.424	0.012	1.500

$$C_f = \frac{2\mu^T \left| \frac{dU}{dr} \right|_{r=R}}{\rho_o U_o^2} \quad (a)$$

$$(C_f)_{lam} = \frac{16}{Re} \quad (b) \quad C_f^* = \frac{C_f}{(C_f)_{lam}} \quad (c) \quad (15)$$

To strengthen the discussions on transition, boundary layer parameters like shape factor ( $H$ ) and intermittency ( $\gamma$ ) (White [30]) are estimated by Eqs. (16a) and (b), respectively. As the laminar ( $H_{lam} = 3.36$ ) and turbulent ( $H_{turb} = 1.70$ ) shape factor values are computed with Eq. (16a), by integrating the laminar [Eq. (14a)] and turbulent [Eq. (14b)] profiles, the shape factor data of the transitional flows were also calculated with Eq. (16a), but with the computationally evaluated corresponding velocity profiles.

$$H = \frac{\int_{r=0}^{r=R} \left( 1 - \frac{U(r)}{U_m} \right) r dr}{\int_{r=0}^{r=R} \frac{U(r)}{U_m} \left( 1 - \frac{U(r)}{U_m} \right) r dr} \quad (a) \quad \gamma = \frac{H_{lam} - H}{H_{lam} - H_{turb}} \quad (b) \quad (16)$$

Combined effects of  $\epsilon$  and  $Re$  on VPs are displayed in Figure 2, for the non-dimensional surface roughness cases of  $\epsilon^* = 0.001, 0.02, \text{ and } 0.05$  and for the Reynolds numbers of  $Re = 100, 500, 1500, \text{ and } 2000$ . It can be seen from the figure that, at  $Re = 100$  even the highest  $\epsilon^*$  of 0.05 was not influential enough to create a shift in the VP from that of the laminar. The corresponding boundary layer parameters are evaluated as  $H = 3.35\text{--}3.31$  and  $\gamma = 0.007\text{--}0.031$  (Table 1) for  $\epsilon^* = 0.001\text{--}0.05$ , indicating the laminar character. The role of surface roughness on the flow characteristics becomes noticeable with the increase of  $Re$ . The highest surface roughness of  $\epsilon^* = 0.05$  resulted in apparent deviations in the VP of  $Re = 500$  case, where the shape factor decreased to  $H = 3.11$ , intermittency and normalized friction coefficient data rose to  $\gamma = 0.151$  and  $C_f^* = 1.116$ , respectively. Although a universal decision has not been achieved, there exists several experimental and numerical investigations considering the transition onset in internal flow problems with surface roughness. A 10% rise in  $C_f$ , which corresponds to  $C_f^* = 1.1$ , above the traditional laminar formula of Eq. (15b) is recognized as an indicator for the transitional activity by many researchers [4, 5, 6, 8, 31]. The present computations pointed out the transitional Reynolds numbers and intermittency values (Table 1) of  $Re_{tra} \approx 1650$  and  $\gamma = 0.132$  for  $\epsilon^* = 0.001$ ,  $Re_{tra} \approx 575$  and  $\gamma = 0.117$  for  $\epsilon^* = 0.02$ , and  $Re_{tra} \approx 450$  and  $\gamma = 0.136$  for  $\epsilon^* = 0.05$ , where the normalized friction coefficients are evaluated as  $C_f^* = 1.1$ . These results not only indicate that roughness accelerates transition to lower Reynolds numbers but also put forward that transition onset can also be determined through intermittency data, where the present computations perceive the  $\gamma$  range of about 0.1–0.15 for transition onset. Moreover, the determined  $Re_{tra}$  values are in harmony with the results of Kandlikar et al. [4] ( $Re_{tra} \approx 1700$  for  $\epsilon^* \approx 0.003$ ), Obot [8] ( $Re_{tra} \approx 2040$  for inconsiderable roughness) and Wu and Little [31] ( $Re_{tra} \approx 510\text{--}1170$  for

a wide range of  $\epsilon^*$ ). Figure 2 additionally demonstrates the growing influence of surface roughness on the flow pattern (VPs) with Reynolds number, especially the near wall regions ( $r/R \geq 0.75$ ) and the centerline ( $r/R = 0$ ). The gap between the  $U_c/U_o$  ratios and the traditional data of  $U_c/U_o = 2.0$  [Eq. (14a)] increases both with higher  $\epsilon^*$  and Re.

Since viscous effects have a considerable impact on entropy generation,  $C_f$  gains higher importance especially due to its direct contribution on the irreversibility distribution ratio [ $\phi$ , Eq. (13b)]. Computational  $C_f^*$  values, for various  $\epsilon^*$  and Re cases, are presented in Figure 3, with the available literature-based data, and also tabulated in Table 1. It can be seen that  $C_f^*$  values augment both with  $\epsilon^*$  and Re, such that as  $C_f^*$  is evaluated as 1.006, 1.028, and 1.088 for Re = 100, 500, and 1500, respectively, at  $\epsilon^* = 0.001$ , and the corresponding values rise to  $C_f^* = 1.021, 1.116, \text{ and } 1.350$  at  $\epsilon^* = 0.05$ . Vicente et al. [5], Guo and Li [6], Engin et al. [9], and Wang et al. [24] also reported the augmenting role of roughness on friction coefficient with Reynolds number. On the other hand, for  $Re < 450$ , in the complete  $\epsilon^*$  set (0.001–0.05), the  $C_f^*$  values are lower than 1.1, which indicates that surface roughness does not create a variation in the frictional characteristics of laminar flow. Figure 3 indicates augmentations in  $C_f^*$  for  $Re > 450$ , specifying that the influence of surface roughness becomes apparent with higher Re, which was also recorded by Guo and Li [6] for microscale flow. Figure 3 additionally puts forward that most of the experimental studies on laminar flows available in the literature reported elevated friction coefficients for  $Re > 500$  (Wu and Little [31], Kohl et al. [32], and Choi et al. [33]); however, the experimental friction factors of Yu et al. [34] were even below the laminar theory for  $100 < Re < 2000$ . The discussions, on micropipe flow characteristics with surface roughness, clarify the impact of surface roughness in laminar flow by putting forward the VP transformation from laminar to the initial stages of transitional character with ascends in  $C_f^*$  and  $\gamma$  and descends in H and  $U_c/U_o$  values.

**Heat Transfer Characteristics**

Figure 4 presents the mean-temperature variation ( $\Delta T = T_{ex} - T_{in}$ ) values of the laminar-transitional flow in the Reynolds number range of  $1 \leq Re \leq 2000$  for three heat flux and non-dimensional surface roughness cases. Computations put forward that the role of  $\epsilon^*$  on  $\Delta T$  is ignorable at low Reynolds numbers. However, the deviations become recognizable in the cases with higher Re where the application of higher surface roughness results in lower mean-temperature variations. The identifiable  $\Delta T$  deviation due to  $\epsilon^*$  can be characterized by  $1\%$  shift among the two limiting  $\epsilon^*$  cases. Formulating the method with the formula of  $(\frac{\Delta T_{\epsilon^*=0.05} - \Delta T_{\epsilon^*=0.001}}{\Delta T_{\epsilon^*=0.001}}) \times 100 = 1$  results in the onset Reynolds numbers of  $Re = 79, 425, \text{ and } 528$  for the heat flux values of  $q'' = 5, 50, \text{ and } 100 \text{ W/m}^2$ , respectively. These limits put forward that higher heat flux values narrows the influential Re range of  $\epsilon^*$  on  $\Delta T$  in laminar flow. Figure 4 further interprets a reverse relation

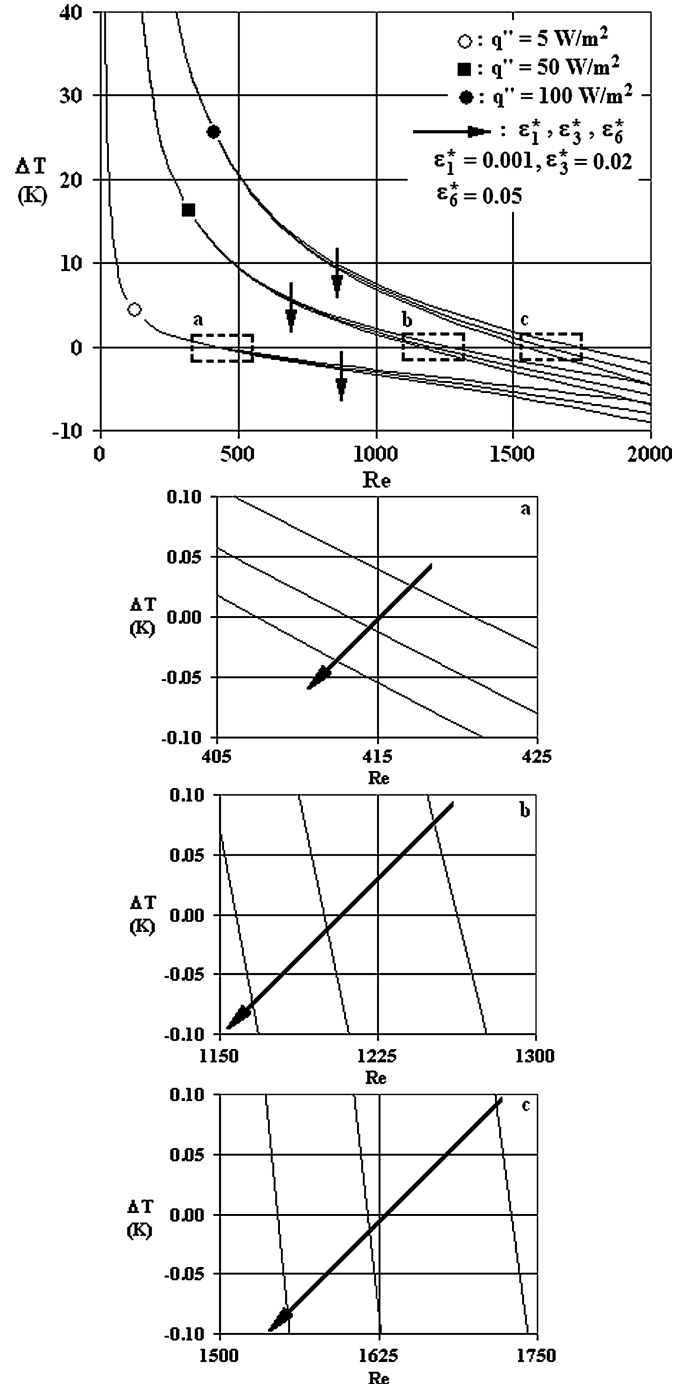


Figure 4 Variations of  $\Delta T$  with Re,  $\epsilon^*$ , and  $q''$ .

among the Re and  $\Delta T$  values, being independent of the intensity of heat flux. This result also indicates that the role of heat flux on mean-temperature variation values is more remarkable at lower mass flow rates. Moreover, augmentations of the heat flux values are accompanied with higher temperature rise data in the complete Reynolds number range. On the other hand, computations point out that the role of heat flux on temperature rise is more remarkable at low Reynolds number cases. Numerically it can more specifically be identified that for the  $q'' = 5 \text{ W/m}^2$

Downloaded By: [TUBITAK EKUAL] At: 08:49 6 May 2009

**Table 2**  $\Psi_{\text{loss}}$  and  $\Delta T$  values for various Re,  $\varepsilon^*$ , and  $q''$  cases

$q''$ (W/m <sup>2</sup> )	5		50		100	
$Q_s$ (W)	$7.85 \times 10^{-3}$		$7.85 \times 10^{-2}$		$1.57 \times 10^{-1}$	
Re = 100						
$\Psi_{\text{loss}}$ (W) ( $\varepsilon_1^* \dots \varepsilon_6^*$ )	$4.38 \times 10^{-4} \dots 4.46 \times 10^{-4}$		$5.63 \times 10^{-4} \dots 5.72 \times 10^{-4}$		$7.34 \times 10^{-4} \dots 7.44 \times 10^{-4}$	
$\Delta T$ (K) ( $\varepsilon_1^* \dots \varepsilon_6^*$ )	5.37 ... 5.35		56.37 ... 56.34		112.62 ... 112.58	
Re = 500						
$\Psi_{\text{loss}}$ (W) ( $\varepsilon_1^* \dots \varepsilon_6^*$ )	$1.11 \times 10^{-2} \dots 1.21 \times 10^{-2}$		$1.17 \times 10^{-2} \dots 1.27 \times 10^{-2}$		$1.24 \times 10^{-2} \dots 1.34 \times 10^{-2}$	
$\Delta T$ (K) ( $\varepsilon_1^* \dots \varepsilon_6^*$ )	-0.47 ... -0.6		9.52 ... 9.36		20.59 ... 20.41	
Re = 1500						
$\Psi_{\text{loss}}$ (W) ( $\varepsilon_1^* \dots \varepsilon_6^*$ )	$1.11 \times 10^{-1} \dots 1.41 \times 10^{-1}$		$1.13 \times 10^{-1} \dots 1.43 \times 10^{-1}$		$1.15 \times 10^{-1} \dots 1.45 \times 10^{-1}$	
$\Delta T$ (K) ( $\varepsilon_1^* \dots \varepsilon_6^*$ )	-4.71 ... -7.99		-1.59 ... -2.91		1.88 ... -3.32	
Re = 2000						
$\Psi_{\text{loss}}$ (W) ( $\varepsilon_1^* \dots \varepsilon_6^*$ )	$2.08 \times 10^{-1} \dots 2.85 \times 10^{-1}$		$2.10 \times 10^{-1} \dots 2.89 \times 10^{-1}$		$2.13 \times 10^{-1} \dots 2.92 \times 10^{-1}$	
$\Delta T$ (K) ( $\varepsilon_1^* \dots \varepsilon_6^*$ )	-6.72 ... -9.03		-4.46 ... -6.86		-1.96 ... -4.45	

case the partial derivative of  $\partial\Delta T/\partial\text{Re}$  attains the values of  $-6.34$ ,  $-0.07$ , and  $-0.004$  for Re of 10, 100, and 1000 respectively, whereas these values rise to  $-48.63$ ,  $-1.25$ , and  $-0.016$  for  $q'' = 100$  W/m<sup>2</sup>. These proportions indicate that the role of Reynolds number, thus mass flow rate, on temperature rise becomes more comprehensible at higher heat flux applications. Figure 4 additionally points out the axial-decrease of mean-flow temperature values, beyond certain Reynolds numbers, in spite of heat addition through the lateral walls of the circular pipe. To provide a deeper insight for the heating/cooling outputs, Table 2 shows the applied flux and the corresponding total surface heat transfer values ( $Q_s$ ), together with the amount of viscous energy loss data ( $\Psi_{\text{loss}}$ ) and mean-temperature variations ( $\Delta T$ ) for four Reynolds numbers and also for the surface roughness range of  $\varepsilon^* = 0.001$  ( $\varepsilon_1^*$ )– $0.05$  ( $\varepsilon_6^*$ ). Viscous energy loss per unit volume is the last term on the right hand side of the energy equation [Eq. (8)]. Since flow velocity does not vary in the streamwise direction ( $\partial U_z/\partial z = 0$ ), due to the incompressible character, viscous energy loss data can be evaluated by the volumetric integral of

$$\Psi_{\text{loss}} = 2\pi \int_0^L \int_0^R U \frac{1}{r} \frac{\partial}{\partial r} (\tau r_{rz}) r \, dr \, dz \quad (17)$$

In the case with  $q'' = 5$  W/m<sup>2</sup>, the total heat added through the duct walls ( $Q_s = 7.85 \times 10^{-3}$  W) is higher than viscous energy loss data of Re = 100 for the complete  $\varepsilon^*$  range ( $\Psi_{\text{loss}} = 4.38 \times 10^{-4}$ – $4.46 \times 10^{-4}$  W), where the resulting  $\Delta T$  values are 5.37–5.35 K. However, with the increase of Reynolds number, energy loss data overwhelm the surface heat addition, such that for Re = 500, the limits of  $\Psi_{\text{loss}}$  and  $\Delta T$  are determined to range from  $1.11 \times 10^{-2}$  W to  $1.21 \times 10^{-2}$  W and from  $-0.47$  K to  $-0.6$  K, respectively. The gap between the  $Q_s$  and  $\Psi_{\text{loss}}$  values is also evaluated to rise in the cases with higher Re (Table 2). Table 2 additionally displays the surface heat addition, energy loss, and the associated mean-temperature variations within the Re range of 100–2000 for  $q''$  of 50–100 W/m<sup>2</sup>. The tabulated data is projected to Figure 4 with augmented cooling behavior with the increase of Reynolds number. Particularly, the thermally critical Reynolds numbers  $[(\text{Re}_{\text{cr}})_{\text{th}}]$  can be visualized through

the zoomed plots of Figure 4 and determined as  $(\text{Re}_{\text{cr}})_{\text{th}} \approx 414 \pm 7$ ,  $\approx 1210 \pm 50$ , and  $\approx 1635 \pm 85$  for  $q'' = 5, 50$ , and  $100$  W/m<sup>2</sup>, respectively, where the lower and upper limits refer to  $\varepsilon_6^* = 0.05$  and  $\varepsilon_1^* = 0.001$ . The computational evaluations put forward that higher heat flux augments  $(\text{Re}_{\text{cr}})_{\text{th}}$ ; moreover the expanded  $(\text{Re}_{\text{cr}})_{\text{th}}$  limits explain the enhanced impact of  $\varepsilon^*$  on  $\Delta T$  values at higher  $q''$ . Morini [11], Koo and Kleinstreuer [12], and Celata et al. [13, 14] also reported energy loss and temperature decrease due to friction in laminar flow. They indicated that viscous dissipation is directly related with Reynolds number where they experimentally and numerically recorded exponential augmentations in energy loss due to high Re; their common findings are wall heating due to viscous dissipation; the dissipated energy resulted in loss of flow temperature even if the surface roughness effects were disregarded. Their results show harmony with the present evaluations on heating/cooling behaviors of Figure 4 and the energy loss data of Table 2.

Figure 5 displays the radial variations of temperature values, in non-dimensional form with respect to the centerline value ( $T_c$ ), for various surface roughness, heat flux and Reynolds numbers. Since the energy loss ( $\Psi_{\text{loss}}$ ) due to viscous dissipation on the solid walls and surface heat transfer rates have considerable influence on temperature profile (TP) development, the computed TPs are displayed in conjunction with the laminar constant heat flux (CHF) formula of Eq. (18) [30].

$$T(r) = T_s - \frac{2U_o \kappa_f^T R^2}{\rho C_p^T} \left( \frac{dT_o}{dz} \right) \left[ \frac{3}{16} + \frac{1}{16} \left( \frac{r}{R} \right)^4 - \frac{1}{4} \left( \frac{r}{R} \right)^2 \right] \quad (18)$$

Computations put forward that the TPs of the flows for Re  $\leq 500$  coincide for the complete  $\varepsilon$  range investigated, designating the insignificant influence of surface roughness at low Re, where the mean-temperature variation discussions of Figure 4 are completely in harmony with this determination. At the lowest heat flux case of  $q'' = 5$  W/m<sup>2</sup>, for Re = 100, the energy loss rates are quite low ( $\Psi_{\text{loss}} \approx 4.4 \times 10^{-4}$  W, see Table 2), resulting in the similar TP to the laminar constant heat flux profile [Eq. (18)]. Nevertheless, at higher heat flux cases ( $q'' = 50$ – $100$  W/m<sup>2</sup>) the flow temperatures rise, causing the flow

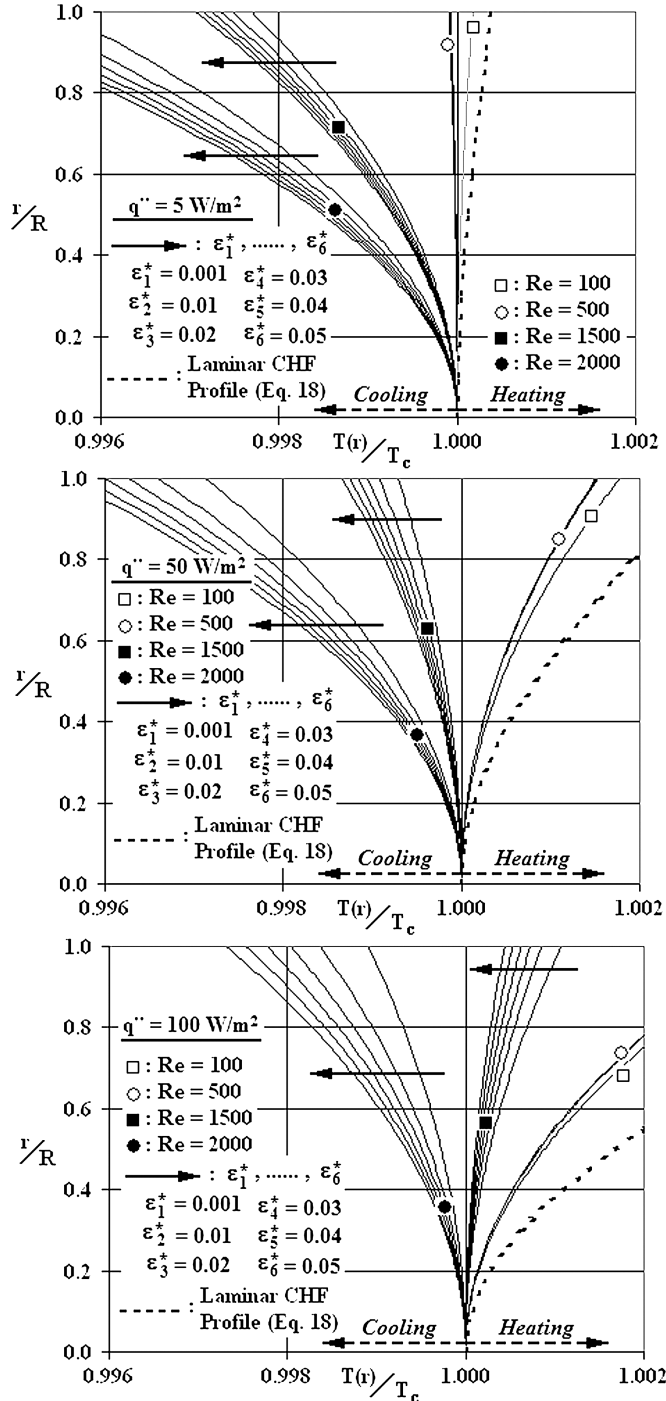


Figure 5 Variations of radial temperature profiles with Re,  $\epsilon^*$ , and  $q''$ .

viscosity values and the energy loss data to rise (Table 2) at the same Reynolds number case of  $Re = 100$ , which result in more evident shifts in TPs from that of Eq. (18). On the other hand, with the increase of Reynolds number ( $Re > 500$ ), and thus flow velocity and mass flow rate, the role of surface roughness becomes apparent with significant variations in the TPs, which can be attributed to the elevated energy loss amounts as given in Table 2. Heating of the flowing air is computed for the con-

dition of  $\Psi_{loss} < Q_s$ , but in the cases with viscous dissipation dominating the surface heat addition ( $\Psi_{loss} > Q_s$ ) cooling is the outcome, where the thermally critical Reynolds numbers are as described in Figure 4. The growing role of  $\epsilon$  with Re, especially in the flows with decreasing mean flow temperatures, is also shown in Figure 5. At the lowest heat flux case of  $q'' = 5 \text{ W/m}^2$  the energy loss data are given as  $\Psi_{loss} = 1.11 \times 10^{-1} - 1.41 \times 10^{-1} \text{ W}$  ( $\epsilon_1^* - \epsilon_6^*$ ) and  $\Psi_{loss} = 2.08 \times 10^{-1} - 2.85 \times 10^{-1} \text{ W}$  for  $Re = 1500$  and  $Re = 2000$ , respectively (Table 2). Although, at the highest heat flux of  $q'' = 100 \text{ W/m}^2$ , these ranges expand to  $\Psi_{loss} = 1.15 \times 10^{-1} - 1.45 \times 10^{-1} \text{ W}$  and  $\Psi_{loss} = 2.13 \times 10^{-1} - 2.92 \times 10^{-1} \text{ W}$ . The augmented viscosity values at higher temperatures can be regarded as the source of the elevated  $\Psi_{loss}$  values with higher heat flux. Moreover, these energy loss ranges also indicate that the gap among the lower and upper  $\Psi_{loss}$  limits enlarge significantly with Reynolds number and secondarily with surface heat flux. In compressible converging nozzle flows, enhanced frictional energy loss records with increase of surface heat flux were also reported by Ozalp [21, 22]. For the complete surface heat flux range considered, at higher Reynolds numbers and surface roughness conditions, the numerical analysis revealed deviations in the TPs from the CHF profile, denoting the augmentation of the viscous dissipation and the associated frictional energy loss rates at high Re and  $\epsilon$ .

Figure 6 presents the combined influences of surface roughness and Reynolds number on Nusselt number, for the ranges of  $\epsilon^* = 0.001 - 0.05$  and  $Re = 1 - 2000$ . Below  $Re = 100$ , surface roughness and flow velocity were determined not to be influential on heat transfer rates, such that the Nusselt number was within the limits of the traditional laminar values for constant heat flux ( $Nu = 4.36$ ) and constant surface temperature ( $Nu = 3.66$ ) cases. Computations indicated a nearly-constant Nu of 4.04 for  $Re < 100$ ; however, with the increase of Re, heat transfer rates are also evaluated to rise. The Vicente et al. [5] heat transfer measurements, showing parallelism with the current evaluations, pointed out constant Nu of  $\sim 4.36$  for

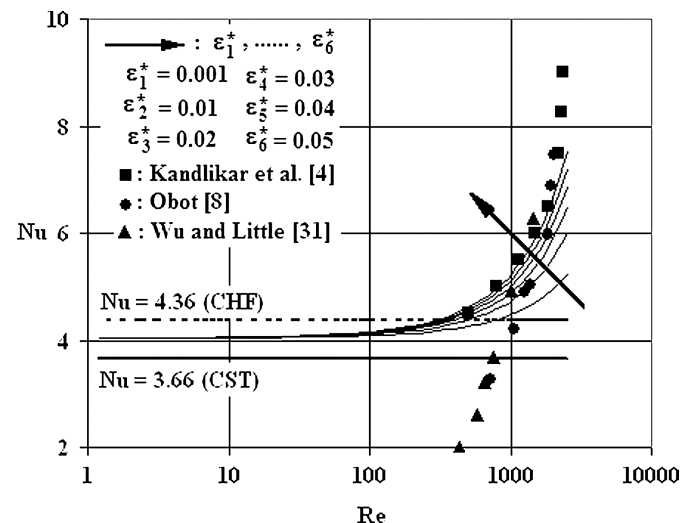


Figure 6 Variation of Nu with Re and  $\epsilon^*$ .

$Re < 700$ , which is followed by an increase in  $Nu$ . It is also determined that surface roughness has an augmenting role on Nusselt number, where the impact becomes apparent for  $Re > 100$ . The present computations resulted in the  $Nu_{\varepsilon^*=0.05}/Nu_{\varepsilon^*=0.001}$  ratios of 1.086, 1.168, and 1.259 for  $Re = 500, 1000$ , and  $1500$ , which clearly denote that the influence of  $\varepsilon^*$  on  $Nu$  grows with  $Re$ , which is in harmony with the experimental reports of Wu and Cheng [10]. Additionally, for the  $\varepsilon^*$  range of 0.0018–0.0028, the Kandlikar et al. [4] experimental records also indicated rise of  $Nu$  with surface roughness. On the other hand, Figure 6 also shows that the experimental data of Kandlikar et al. [4] (for  $Re \geq 500$ ), Obot [8] (for  $Re \geq 1000$ ), and Wu and Little [31] (for  $Re \geq 1000$ ) are reasonably in harmony with the current numerical outputs. However, Wu and Little's [31] heat transfer data are lower than the present evaluations for  $Re < 1000$ . Many recent related studies [4, 5, 8, 31] consider 15–20% rise in  $Nu$  with  $Re$  as an indicator for transition, pointing out that augmentations in heat transfer rates with Reynolds number are also significant from the point of transition. Applying the transitional Reynolds numbers of Figure 2, the computational heat transfer evaluations indicate the  $Nu_{Re_{tra}}/Nu_{Re=1}$  ratios of 1.18 ( $Re_{tra} = 1650, \varepsilon^* = 0.001$ ), 1.12 ( $Re_{tra} = 575, \varepsilon^* = 0.02$ ), and 1.11 ( $Re_{tra} = 450, \varepsilon^* = 0.05$ ). These proportions not only put forward the computational matching of the flow and heat transfer characteristics, but also confirm the parallelism of the present results with the transitional reports of [4, 5, 8, 31].

## 2ND LAW ANALYSES

### Entropy Generation

Figure 7 displays the variation of entropy generation ( $S$ ) with mass flow rate ( $\dot{m}$ ) and mean-temperature variation ( $\Delta T$ ) for the heat flux cases of  $q'' = 5, 50$ , and  $100 \text{ W/m}^2$  and for the fixed

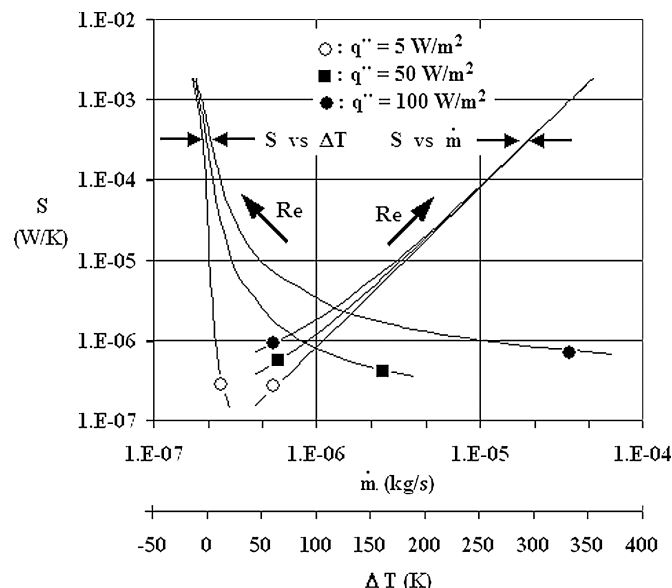


Figure 7 Variations of  $S$  with  $\dot{m}$  and  $\Delta T$  for various  $q''$  cases at  $\varepsilon^* = 0.02$ .

surface roughness of  $\varepsilon^* = 0.02$ . Figure 7 indicates that there exists almost a linear relation among  $S$  and  $\dot{m}$ , where Richardson et al. [15], in a microchannel with  $D_h = 0.61 \text{ mm}$ , similarly reported a linear relationship among  $S$  and  $Re$  on a log–log basis. Moreover, the impact of  $q''$  becomes identifiable at low Reynolds numbers, such that the  $(\frac{S_{Q=100 \text{ W/m}^2} - S_{Q=5 \text{ W/m}^2}}{S_{Q=5 \text{ W/m}^2}}) \times 100$  ratio attains the values of 78.43%, 8.96%, 2.14%, and 1.35% for  $Re = 100, 500, 1500$ , and  $2000$  respectively. On the other hand, the growth of  $S$  with  $Re$  validates the augmentation of the loss of available energy from the flow domain by means of entropy generation, which results in the cooling character evaluated at high Reynolds numbers (Figures 4 and 5). This record puts forward that to attain the expected flow temperature rise levels, surface heat flux values must be decided by also considering the total entropy generation within the flow environment. The tabulated data (Table 3) of entropy generation for the Reynolds number and surface roughness ranges of  $Re = 100$ – $2000$  and  $\varepsilon^* = 0.001$ – $0.05$  coincide with Figure 7 and interpret additional findings. It can be found by inspecting Table 3 that surface roughness has no role on entropy values at low  $Re$ , whereas the deviations become apparent at higher  $Re$ . As the ratio of  $(\frac{S_{\varepsilon^*=0.05} - S_{\varepsilon^*=0.001}}{S_{\varepsilon^*=0.001}}) \times 100$  gets the values of 0.52% ( $Re = 500$ ), 4.93% ( $Re = 1500$ ), and 9.39% ( $Re = 2000$ ) at  $q'' = 5 \text{ W/m}^2$ , they decrease to 0.48%, 4.82%, and 9.10% at  $q'' = 100 \text{ W/m}^2$ . These ratios suggest that the influence of  $\varepsilon^*$  on  $S$  is more remarkable at low heat flux applications. Figure 7 additionally shows that entropy generation is inversely proportional to the mean-temperature variation data. The effects of  $\Delta T$  on  $S$  are more significant at high  $Re$  with considerable drops in  $S$  with the rise of  $\Delta T$ . On the other hand, especially at high heat flux cases ( $q'' = 50$ – $100 \text{ W/m}^2$ ) the trends become almost asymptotic at the lower limit of the investigated Reynolds number range ( $Re = 1$ ), indicating that the impact of  $\Delta T$  on  $S$  becomes negligible at high  $\Delta T$  (low  $Re$ ) cases.

A deeper inspection into the entropy mechanism can be performed by decomposing the overall generation rate into subsections. Figure 8 is prepared to display the cross-correlations of the thermal ( $S_{\Delta T}$ ) and frictional ( $S_{\Delta P}$ ) parts of the total entropy generation for various surface roughness, heat flux, and Reynolds number cases. It can be seen from the figure that as  $S_{\Delta P}$  rises at the end of heating period, which can be attributed to the surface roughness effects, minor reductions are determined in  $S_{\Delta T}$ . This interaction is common for all heat flux cases; however, the onset of the defined region varies. Since  $S_{\Delta P}$  is directly associated with velocity, mass flow rate, and Reynolds number, frictional entropy generation values are computed to increase continuously with  $Re$ . As surface roughness creates a decreasing impact on thermal entropy generation at the end of heating period [below the thermally critical Reynolds numbers of  $(Re_{cr})_{th} \approx 414, 1210$  and  $1635$  for  $q'' = 5, 50$  and  $100 \text{ W/m}^2$  respectively], above  $(Re_{cr})_{th}$  surface roughness augments the thermal entropy generation values. On the other hand, Table 3 displays the augmenting role of higher heat flux applications on the entropy generation rates. As the ratio of  $S_{Q=50 \text{ W/m}^2}/S_{Q=5 \text{ W/m}^2}$  is 1.29

**Table 3** S values for various Re,  $\epsilon^*$ , and  $q''$  cases

$q''$ (W/m <sup>2</sup> )	S (W/K) ( $\epsilon_1^* \dots \epsilon_6^*$ )					
	5		50		100	
Re = 100	$1.53 \times 10^{-6}$	$1.53 \times 10^{-6}$	$1.98 \times 10^{-6}$	$1.98 \times 10^{-6}$	$2.73 \times 10^{-6}$	$2.3 \times 10^{-6}$
Re = 500	$3.84 \times 10^{-5}$	$3.86 \times 10^{-5}$	$3.98 \times 10^{-5}$	$4.01 \times 10^{-5}$	$4.19 \times 10^{-5}$	$4.21 \times 10^{-5}$
Re = 1500	$3.65 \times 10^{-4}$	$3.83 \times 10^{-4}$	$3.68 \times 10^{-4}$	$3.86 \times 10^{-4}$	$3.73 \times 10^{-4}$	$3.91 \times 10^{-4}$
Re = 2000	$6.71 \times 10^{-4}$	$7.34 \times 10^{-4}$	$6.76 \times 10^{-4}$	$7.38 \times 10^{-4}$	$6.81 \times 10^{-4}$	$7.43 \times 10^{-4}$

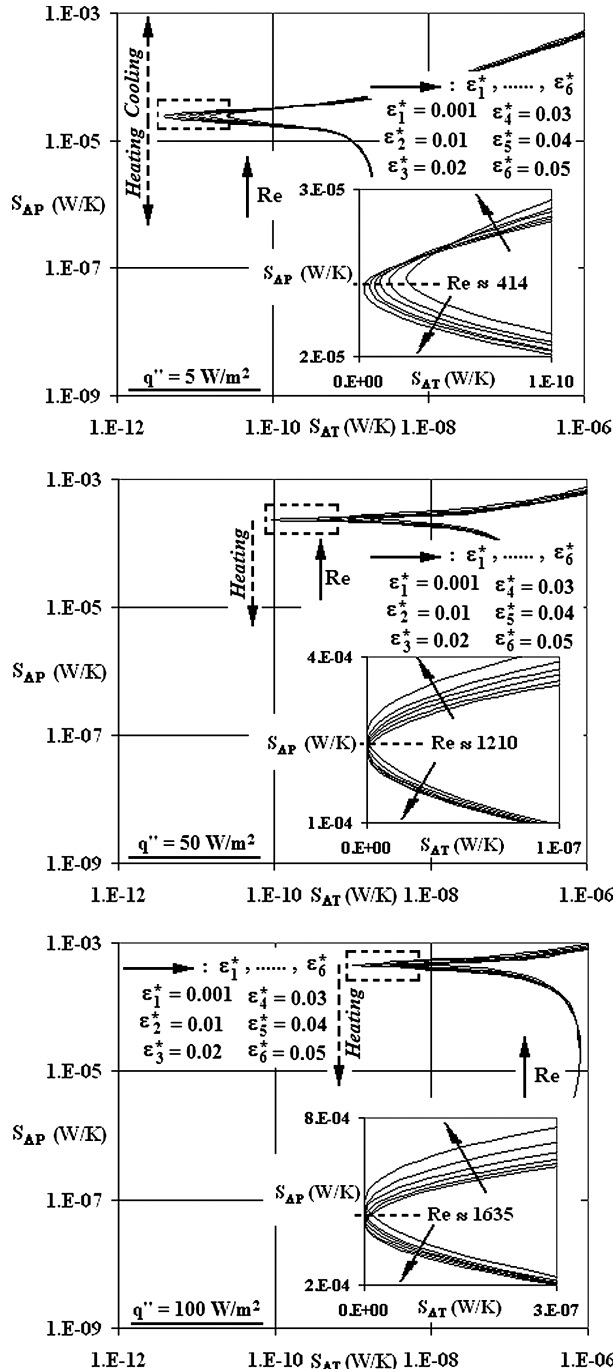


**Figure 8**  $S_{\Delta T}$  vs  $S_{\Delta P}$  for various Re,  $\epsilon^*$ , and  $q''$  cases.

at Re = 100, it decreases to  $\sim 1.0064$  at Re = 2000. The low ratio at Re = 2000 is due to the slightly higher temperature values ( $\sim 2^\circ\text{C}$ , Figure 4) at  $q'' = 50 \text{ W/m}^2$ , which causes minor grows in flow viscosity, frictional activity, and  $S_{\Delta P}$ . It can additionally be inspected from Figure 8 that, with the increase of Reynolds number,  $S_{\Delta P}$  becomes dominant over  $S_{\Delta T}$  by occupying the major portion in the overall entropy generation. Moreover, augmentations in either  $S_{\Delta T}$  or  $S_{\Delta P}$  are also recognizable in the upper segment of the considered Re range.

**Irreversibility Distribution Ratio**

Besides the discussions on total, thermal, and frictional entropy generations, dependence of local irreversibility distribution ratio ( $\phi'''$ ) on Reynolds number, and total irreversibility distribution ratio ( $\phi$ ) on mass flow rate, for different surface roughness and heat flux cases needs further investigation. It can be seen from Figure 9 that the local irreversibility distribution ratio becomes trivial at the centerline ( $r/R = 0$ ) of the pipe, in the complete set of flow scenarios considered, being independent of Re,  $\epsilon^*$  and  $q''$ . This result not only puts forward that the frictional activity ( $S_{\Delta P}'''$ ) is negligible in the centerline region, but also indicates that the major portion of the total entropy generation is thermal based ( $S_{\Delta T}'''$ ). On the other hand, the highest  $\phi'''$  values are computed at the solid wall ( $r/R = 1$ ), which can be detailed by the considerable frictional activity and by the elevated velocity gradients near the solid boundary (Figure 2). It can additionally be found by inspecting Figure 9 that in the cooling scenarios of  $q'' = 5 \text{ W/m}^2$  for  $Re \geq 414$ ,  $q'' = 50 \text{ W/m}^2$  for  $Re \geq 1210$ , and  $q'' = 100 \text{ W/m}^2$  for  $Re \geq 1635$  (Figure 4), the local values of the irreversibility distribution ratio data, in the entire radial domain ( $0 < r/R < 1$ ), decrease with higher surface roughness. However, in the heating scenarios, frictional activity augments in the regions close to the pipe walls, resulting in the  $S_{\Delta P}'''$  portion to increase in the total generation, which can be attributed to the locally raised viscosity values due to high wall temperatures. It can be concluded that the impact of surface roughness on the local irreversibility distribution ratio values is contrary at the centerline ( $r/R = 0$ ) and on the solid wall ( $r/R = 1$ ). It can specifically be indicated that for  $q'' = 50 \text{ W/m}^2$ , as the radial region of the increasing role of  $\epsilon^*$  on  $\phi'''$ , due to heating, is  $0.77 \leq r/R \leq 1$  for Re = 500, the corresponding one is  $0.54 \leq r/R \leq 1$  for Re = 1000. Although at the heat flux of  $q'' = 100 \text{ W/m}^2$  for Re = 500, 1000, and 1500 these radial

Downloaded By: [TUBTAK EKUAL] At: 08:49 6 May 2009

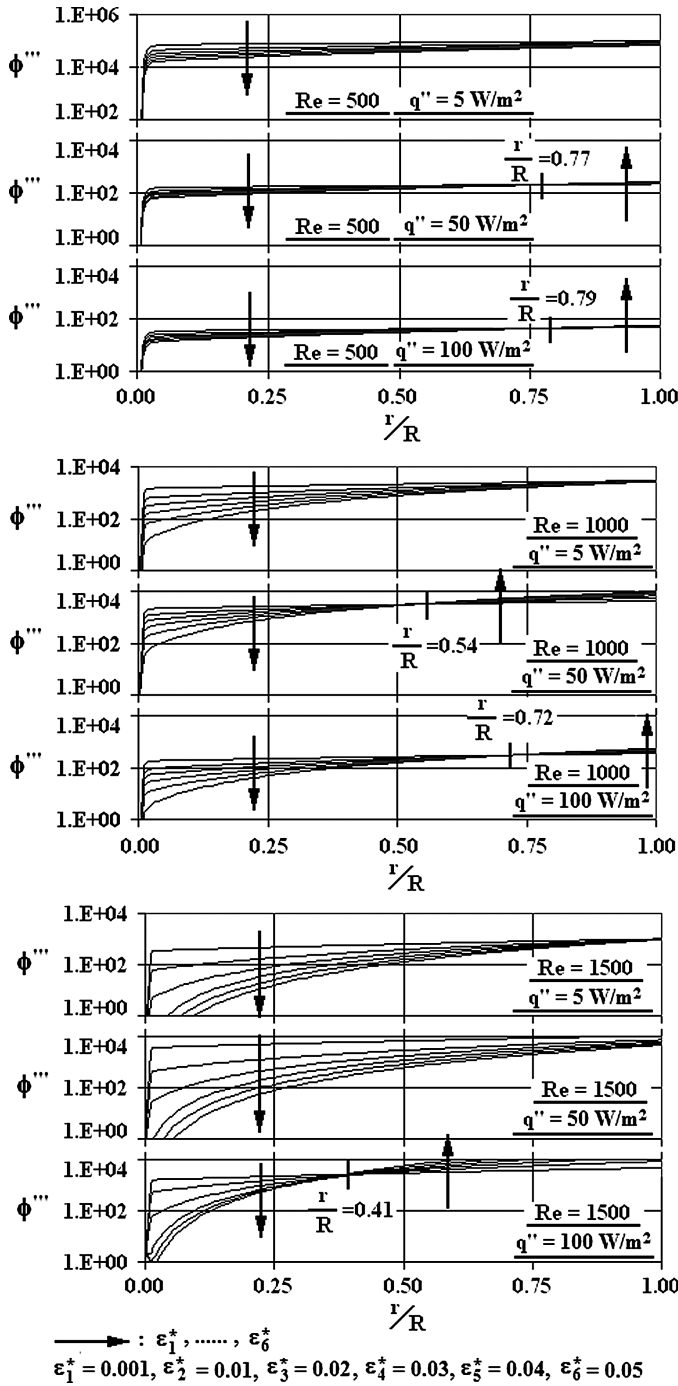


Figure 9 Variations of radial  $\phi'''$  profiles for various  $Re$ ,  $\varepsilon^*$ , and  $q''$  cases.

zones become  $0.79 \leq r/R \leq 1$ ,  $0.72 \leq r/R \leq 1$ , and  $0.41 \leq r/R \leq 1$ , respectively. These radial boundaries clearly put forward that the near-wall increasing role of  $\varepsilon^*$  on  $\phi'''$  becomes stronger with Reynolds number for fixed heat flux values. The radially expanding character becomes recognizable especially in the cases of  $Re = 500-1000$  for  $q'' = 50 \text{ W/m}^2$  and  $Re = 1000-1500$  for  $q'' = 100 \text{ W/m}^2$ .

Figure 10 shows that, in heating scenarios, mass flow rate (Reynolds number) and surface roughness decrease the ther-

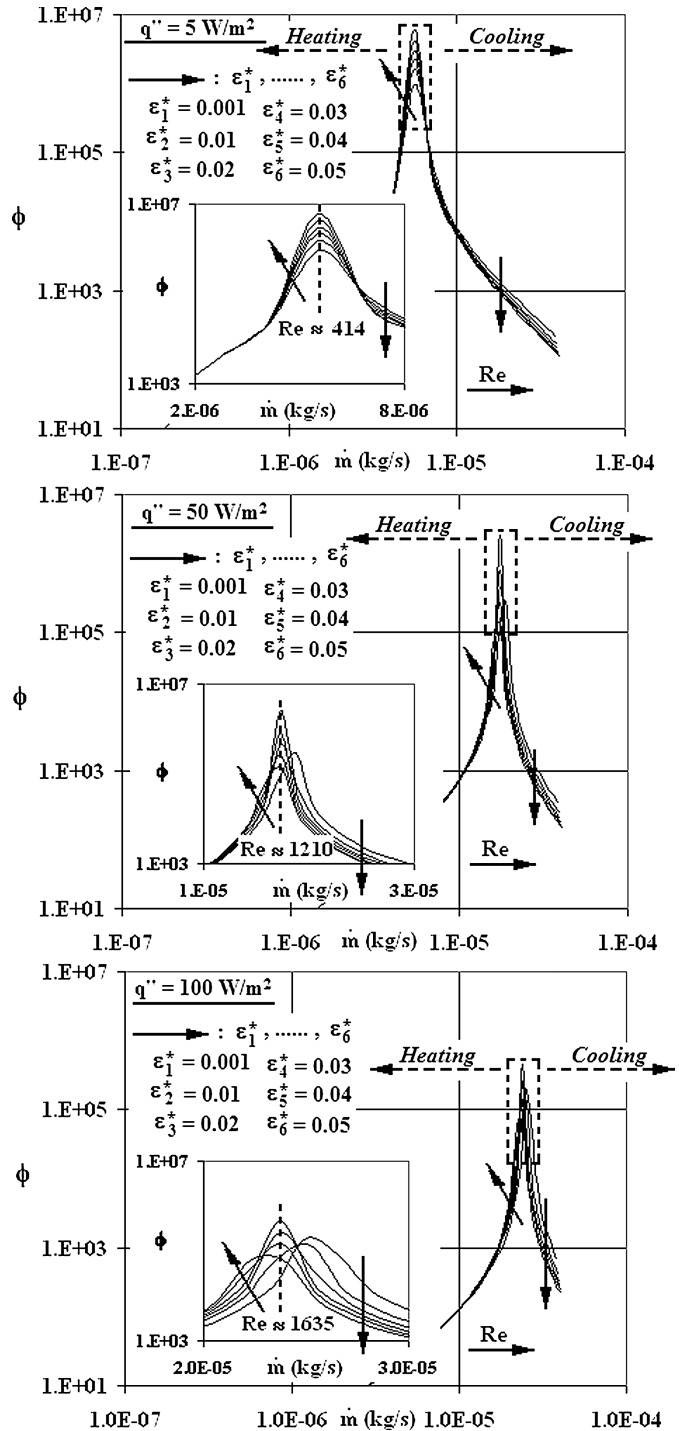


Figure 10 Variations of  $\phi$  values with  $\dot{m}$  for various  $Re$ ,  $\varepsilon^*$ , and  $q''$  cases.

mal entropy generation, whereas the opposite is evaluated for the frictional entropy generation. The augmentations in  $S_{\Delta P}$  are more considerable when compared with the decrease rates of  $S_{\Delta T}$  (Figure 8), which result in significant increase rates in  $\phi$ . Since the frictional entropy generation is substantially dominant to thermal entropy generation (Figure 8), the increase trends in  $S_{\Delta P}$  with  $Re$  directly specify  $S$  variations with mass flow rate (Figure 7) and with  $Re$  (Table 3). The determined character is

similar in all heat flux applications, in spite of the variation of the defined Re range. Present computational determinations are completely in harmony with Ko's [18] results, for double-sine ducts, on the variations of  $S_{\Delta T}$  and  $S_{\Delta P}$  with Re, and with the results of Sahin et al. [26], for a circular heat exchanger tube, on the variations of  $S_{\Delta T}$  and  $S_{\Delta P}$  with  $\varepsilon^*$ . Figure 10 additionally indicates that the role of  $\varepsilon^*$  on  $\phi$  becomes apparent toward the end of heating period, and thus augmentations are observed in  $\phi$  with  $\varepsilon^*$  in heating and the contrary outcome is evaluated in cooling scenarios. As there exists a direct link among velocity–mass flow rate–Reynolds number with frictional entropy generation,  $S_{\Delta P}$  values are computed to continuously rise with Re, where the augmentations become more recognizable in higher Re. Figures 8 and 10 put forward that minimum thermal entropy generation values ( $S_{\Delta T} = 1.1 \times 10^{-11}$  W/K) are evaluated at  $Re = (Re_{cr})_{th}$ , at the end of the decreasing trend in heating period with Re, resulting in the maximum  $\phi$  values [ $q'' = 5$  W/m<sup>2</sup> with  $(Re_{cr})_{th} = 414$  and  $\phi = 2.26 \times 10^6$ ,  $q'' = 50$  W/m<sup>2</sup> with  $(Re_{cr})_{th} = 1210$  and  $\phi = 2.19 \times 10^7$ ,  $q'' = 100$  W/m<sup>2</sup> with  $(Re_{cr})_{th} = 1635$  and  $\phi = 4.08 \times 10^7$ ] of the complete Re range. On the other hand,  $\phi$  values are computed to decrease for  $Re > (Re_{cr})_{th}$  (Figure 10), which can be attributed to the sharper increase rates in  $S_{\Delta T}$  than those of  $S_{\Delta P}$  above the thermally critical Reynolds numbers. Besides, computations put forward that  $S_{\Delta P}$  values increase with heat flux both in heating and cooling cases; however,  $S_{\Delta T}$  data are evaluated to increase in heating and to decrease in cooling scenarios with surface heat flux. Moreover, as the  $\phi$  values are determined to decrease with  $q''$  and to increase with Re in heating [ $Re \leq (Re_{cr})_{th}$ ], they are computed to increase with heat flux and to decrease with Reynolds number in cooling [ $Re \geq (Re_{cr})_{th}$ ]. The results of Ko [17] for a helical coil, on the interaction of  $\phi$  with  $q''$  and Re, are completely in harmony with the current computations.

## CONCLUSIONS

First and 2nd law characteristics of laminar-transitional flow in a micropipe have been presented in detail. Integrated effects of surface roughness, heat flux, and Reynolds number are investigated by the simultaneous solution of temperature dependent property continuity, momentum, and energy equations.

First law analysis points to the following major results:

Surface roughness is evaluated to accelerate transition to lower Reynolds numbers with flatter velocity profiles, lower shape factors, and higher normalized friction coefficient and intermittency values. As the role of Reynolds number on mean-temperature variation is computed to become more comprehensible at higher heat flux cases, due to viscous dissipation, thermo-critical Reynolds numbers are determined, beyond which the frictional energy loss data are above the surface heat addition values. Nusselt number is determined to augment with surface roughness, where the impact becomes apparent for  $Re > 100$ . Such that the  $Nu_{\varepsilon^*=0.05}/Nu_{\varepsilon^*=0.001}$  ratio attains the values

of 1.086, 1.168, and 1.259 for  $Re = 500, 1000,$  and  $1500$ , revealing that the influence of surface roughness on Nusselt number grows with Reynolds number.

The main findings of 2nd law investigations can be summarized as:

The impact of heat flux on entropy generation is identifiable at low Reynolds numbers. However, the contrary is valid for the role of surface roughness on entropy, where the influence is more remarkable at low heat flux. It is evaluated that higher heat flux enhances entropy generation at low Reynolds numbers, whereas surface roughness creates an increasing impact on thermal entropy generation in cooling scenarios. It is further determined that, to attain the expected flow temperature rise levels, entropy generation must also be considered in conjunction with surface heat flux values. Thermal and frictional entropy generation data are computed to augment recognizably in the upper segment of the considered Reynolds number range. The considerable frictional activity and the elevated velocity gradients near the solid boundary resulted in the highest radial irreversibility distribution ratio values in that region. The radial irreversibility distribution ratio data are computed to decrease with surface roughness in the entire radial domain in cooling scenarios. However, in heating, frictional entropy generation and thus irreversibility distribution ratio are evaluated to grow with surface roughness in the regions close to the pipe walls. It is additionally determined that the near-wall increasing role of surface roughness on irreversibility distribution ratio becomes stronger with Reynolds number for fixed heat flux. As the thermally critical Reynolds numbers pointed not only to minimum thermal entropy generation data but also to maximum irreversibility distribution ratio values, heat flux is determined to increase the frictional entropy generation values.

## NOMENCLATURE

a	curve fit constants
A	cross-sectional area, m <sup>2</sup>
$C_f$	friction coefficient
$C_f^*$	normalized friction coefficient
$C_v$	constant-volume specific heat, J/kgK
$C_p$	constant-pressure specific heat, J/kgK
D	diameter, m
$\Delta T$	mean-temperature variation, K
e	internal energy per unit mass, J/kg
$f_\varepsilon(z)$	surface roughness model function
h	convective heat transfer coefficient, W/m <sup>2</sup> K
H	shape factor
k	kinetic energy per unit mass, J/kg
L	pipe length, m
$\dot{m}$	mass flow rate, kg/s
M	Mach number
Nu	Nusselt number
P	static pressure, Pa

$q''$	surface heat flux, $W/m^2$
$q_r''$	radial heat flux, $W/m^2$
$q_z''$	axial heat flux, $W/m^2$
$Q_s$	total surface heat transfer, W
$r$	radial direction
$R$	radius, m; gas constant, J/kgK
$Re$	Reynolds number
$S$	total entropy generation, W/K
$S_{\Delta P}$	total frictional entropy generation, W/K
$S_{\Delta T}$	total thermal entropy generation, W/K
$t$	time, s
$T$	temperature, K
$U$	axial velocity, m/s
$\vec{V}$	velocity vector, m/s
$z$	axial direction

### Greek Symbols

$\varepsilon$	roughness amplitude, mm
$\varepsilon^*$	non-dimensional surface roughness ( $= \varepsilon/D$ )
$\delta_i$	Kronecker unit tensor
$\phi$	irreversibility distribution ratio
$\kappa_f$	thermal conductivity of fluid, W/mK
$\gamma$	intermittency
$\mu$	dynamic viscosity, Pa.s
$\nu$	kinematic viscosity, $m^2/s$
$\theta$	peripheral direction
$\rho$	density, $kg/m^3$
$\tau$	shear stress, Pa
$\xi$	air properties
$\Psi_{\text{loss}}$	energy loss, W
$\omega$	roughness period, mm
$\omega'$	roughness periodicity parameter ( $= \omega/\varepsilon$ )

### Subscripts

c	center
cr	critical
ex	exit
h	hydraulic
in	inlet
lam	laminar
o	mean
$r, \theta, z$	radial, peripheral, axial
s	surface
th	thermal
tra	transitional
turb	turbulent
w	wall

### Superscripts

''	local rate
T	temperature dependency

### REFERENCES

- [1] Ozgener, L., Hepbasli, A., and Dincer, I., Parametric Study of the Effect of Reference State on Energy and Exergy Efficiencies of Geothermal District Heating Systems (GDHSs): An Application of the Salihli GDHS in Turkey, *Heat Transfer Engineering*, vol. 28, pp. 357–364, 2007.
- [2] Yilbas, B. S., and Pakdemirli, M., Entropy Generation Due to the Flow of a Non-Newtonian Fluid with Variable Viscosity in a Circular Pipe, *Heat Transfer Engineering*, vol. 26, pp. 80–86, 2005.
- [3] Stewart, S. W., Shelton, S. V., and Aspelund, K. A., Finned-Tube Heat Exchanger Optimization Methodology, *Heat Transfer Engineering*, vol. 26, pp. 22–28, 2005.
- [4] Kandlikar, S. G., Joshi, S., and Tian, S., Effect of Surface Roughness on Heat Transfer and Fluid Flow Characteristics at Low Reynolds Numbers in Small Diameter Tubes, *Heat Transfer Engineering*, vol. 24, pp. 4–16, 2003.
- [5] Vicente, P. G., Garcia, A., and Viedma, A., Experimental Study of Mixed Convection and Pressure Drop in Helically Dimpled Tubes for Laminar and Transition Flow, *International Journal of Heat and Mass Transfer*, vol. 45, pp. 5091–5105, 2002.
- [6] Guo, Z. Y., and Li, Z. X., Size Effect on Microscale Single-Phase Flow and Heat Transfer, *International Journal of Heat and Mass Transfer*, vol. 46, pp. 149–159, 2003.
- [7] Wen, M. Y., Jang, K. J., and Yang, C. C., Augmented Heat Transfer and Pressure Drop of Strip-Type Inserts in the Small Tubes, *Heat and Mass Transfer*, vol. 40, pp. 133–141, 2003.
- [8] Obot, N. T., Toward a Better Understanding of Friction and Heat/Mass Transfer in Microchannels—A Literature Review, *Microscale Thermophysical Engineering*, vol. 6, pp. 155–173, 2002.
- [9] Engin, T., Dogruer, U., Evrensel, C., Heavin, S., and Gordaninejad, F., Effect of Wall Roughness on Laminar Flow of Bingham Plastic Fluids through Microtubes, *Journal of Fluids Engineering—ASME Transactions*, vol. 126, pp. 880–883, 2004.
- [10] Wu, H. Y., and Cheng, P., An Experimental Study of Convective Heat Transfer in Silicon Microchannels with Different Surface Conditions, *International Journal of Heat and Mass Transfer*, vol. 46, pp. 2547–2556, 2003.
- [11] Morini, G. L., Viscous Heating in Liquid Flows in Microchannels, *International Journal of Heat and Mass Transfer*, vol. 48, pp. 3637–3647, 2005.
- [12] Koo, J., and Kleinstreuer, C., Viscous Dissipation Effects in Microtubes and Microchannels, *International Journal of Heat and Mass Transfer*, vol. 47, pp. 3159–3169, 2004.
- [13] Celata, G. P., Cumo, M., McPhail, S., and Zummo, G., Characterization of Fluid Dynamic Behaviour and Channel Wall Effects in Microtube, *International Journal of Heat and Fluid Flow*, vol. 27, pp. 135–143, 2006.
- [14] Celata, G. P., Morini, G. L., Marconi, V., McPhail, S. J., and Zummo, G., Using Viscous Heating to Determine the Friction Factor in Microchannels—An Experimental Validation, *Experimental Thermal and Fluid Science*, vol. 30, pp. 725–731, 2006.

- [15] Richardson, D. H., Sekulic, D. P., and Campo, A., Low Reynolds Number Flow Inside Straight Micro Channels with Irregular Cross Sections, *Heat and Mass Transfer*, vol. 36, pp. 187–193, 2000.
- [16] Ratts, E. B., and Raut, A. G., Entropy Generation Minimization of Fully Developed Internal Flow with Constant Heat Flux, *Journal of Heat Transfer—ASME Transactions*, vol. 126, pp. 656–659, 2004.
- [17] Ko, T. H., Numerical Investigation of Laminar Forced Convection and Entropy Generation in a Helical Coil with Constant Wall Heat Flux, *Numerical Heat Transfer Part A*, vol. 49, pp. 257–278, 2006.
- [18] Ko, T. H., Numerical Analysis of Entropy Generation and Optimal Reynolds Number for Developing Laminar Forced Convection in Double-Sine Ducts with Various Aspect Ratios, *International Journal of Heat and Mass Transfer*, vol. 49, pp. 718–726, 2006.
- [19] Sahin, A. Z., Second-Law Analysis of Laminar Viscous Flow through a Duct Subjected to Constant Wall Temperature, *Journal of Heat Transfer—ASME Transactions*, vol. 120, pp. 77–83, 1998.
- [20] Kotas, T. J.; Mayhew, Y. R., and Raichura, R. C., Nomenclature for Exergy Analysis, *Proceedings of the Institution of Mechanical Engineers—Part A*, vol. 209, pp. 275–280, 1995.
- [21] Ozalp, A. A., A Computational Study to Predict the Combined Effects of Surface Roughness and Heat Flux Conditions on Converging-Nozzle Flows, *Transactions of the Canadian Society for Mechanical Engineering*, vol. 29, pp. 67–80, 2006.
- [22] Ozalp, A. A., Parallel Effects of Acceleration and Surface Heating on Compressible Flow: Simulation of an Aerospace Propulsion Nozzle with a Medium Amount of Surface Wear, *Strojnicki Vestnik—Journal of Mechanical Engineering*, vol. 53, pp. 3–12, 2007.
- [23] Sheikh, A. K., Zubair, S. M., Younas, M., and Budair, M. O., Statistical Aspects of Fouling Processes, *Proceedings of the Institution of Mechanical Engineers—Part E*, vol. 215, pp. 331–354, 2001.
- [24] Wang, H., Wang, Y., and Zhang, J., Influence of Ribbon Structure Rough Wall on the Microscale Poiseuille Flow, *Journal of Fluids Engineering—ASME Transactions*, vol. 127, pp. 1140–1145, 2005.
- [25] Cao, B. Y., Chen, M., and Guo, Z. Y., Effect of Surface Roughness on Gas Flow in Microchannels by Molecular Dynamics Simulation, *International Journal of Engineering Science*, vol. 44, pp. 927–937, 2006.
- [26] Sahin, A. Z., Zubair, S. M., Al-Garni, A. Z., and Kahraman, R., Effect of Fouling on Operational Cost in Pipe Flow Due to Entropy Generation, *Energy Conversion and Management*, vol. 41, pp. 1485–1496, 2000.
- [27] Incropera, F. P., and DeWitt, D. P., *Fundamentals of Heat and Mass Transfer*, Wiley, New York, 2001.
- [28] Wu, J. S., and Tseng, K. C., Analysis of Micro-Scale Gas Flows with Pressure Boundaries Using Direct Simulation Monte Carlo Method, *Computers and Fluids*, vol. 30, pp. 711–735, 2001.
- [29] Ozalp, A. A., Numerical Analysis of Choked Converging Nozzle Flows with Surface Roughness and Heat Flux Conditions, *Sadhana-Acad. Proc. Engineering*, vol. 31, pp. 31–46, 2006.
- [30] White, F. M., *Fluid Mechanics*, McGraw-Hill, Singapore, 1988.
- [31] Wu, P., and Little, W. A., Measurement of Friction Factors for the Flow of Gases in Very Fine Channels Used for Microminiature Joule–Thompson Refrigerators, *Cryogenics*, vol. 23, pp. 273–277, 1983.
- [32] Kohl, M. J., Abdel-Khalik, S. I., Jeter, S. M., and Sadowski, D. L., An Experimental Investigation of Microchannel Flow with Internal Pressure Measurements, *International Journal of Heat and Mass Transfer*, vol. 48, pp. 1518–1533, 2005.
- [33] Choi, S. B., Barron, R. F., and Warrington, R. O., Fluid Flow and Heat Transfer in Microtubes, *Micromechanical Sensors, Actuators and Systems*, vol. 32, pp. 123–134, 1991.
- [34] Yu, D., Warrington, R., Baron, R., and Ameel, T., An Experimental and Theoretical Investigation of Fluid Flow and Heat Transfer in Microtubes, *ASME/JSME Thermal Engineering Conference*, pp. 523–530, 1995.



**A. Alper Ozalp** is an associate professor in the Thermodynamics Division of the Mechanical Engineering Department of Uludag University in Bursa, Turkey. His research interests include energy–exergy analysis of thermo-fluid systems, experimental and computational fluid mechanics and heat transfer applications, compressible nozzle flows, hydrodynamic lubrication of slider bearings, and engineering software development. Besides being an active reviewer of several SCI journals, he has published several research articles in various peer-refereed international journals and conferences. He is a member of International Association of Engineers, New York Academy of Sciences, and International Who Is Who of Professionals and also the Supervisor/Reviewer/Panelist of Scientific and Technological Research Council of Turkey.